Frequency and Time-Resolved Triply Vibrationally Enhanced Four-Wave Mixing Spectroscopy

Kent A. Meyer and John C. Wright*

Department of Chemistry, University of Wisconsin, Madison, Wisconsin 53706

David E. Thompson

Department of Chemistry, Lawrence University, Appleton, Wisconsin 54912

Received: August 26, 2004; In Final Form: September 28, 2004

We report a two-color frequency domain triply vibrationally enhanced (TRIVE) four-wave mixing (FWM) method that is fully resonant and provides coherent multidimensional vibrational spectra. Temporal and spectral discrimination allow control of the coherent interference of multiple pathways including isolation of a specific pathway and coherent control of the relative intensities of peaks in a 2D spectrum. The method is the coherent analogue to two-color pump−probe spectroscopy and allows the dissection of the individual pathways.

Introduction

The coherent multidimensional vibrational spectroscopy analogues of multidimensional NMR promise to provide the selectivity and resolution of modern NMR methods to vibrational spectroscopy.[1−3] Coherent multidimensional vibrational methods rely on simultaneously exciting two vibrational modes to create a double quantum coherence that is analogous to the double spin coherences in multidimensional NMR.[4,5] Heterodyned stimulated photon echo and related methods are fully resonant four-wave mixing (FWM) methods that generate double vibrational quantum coherences in the time domain using ultrafast fields with defined phase relationships and sufficient bandwidth to span the frequencies of the desired resonances.[6−10] Frequency domain methods are complementary methods that use longer pulses to excite vibrational modes with frequency differences exceeding the excitation fields' bandwidth. The phase relationships between beams are important for establishing the excited coherences that emit in the phase-matched direction. In this paper, we use triply vibrationally enhanced (TRIVE) four-wave mixing,[11,12] a hybrid method in which three tunable infrared excitation beams (two with the same frequency) are each resonant with vibrational transitions. Multidimensional spectra result from scanning the excitation frequencies and spectrally resolving the output signal. The time delays and output frequency can be fixed to isolate individual coherence pathways, whereas other choices permit amplitude-level interference that can coherently control the relative intensity of cross peaks. Because it is a frequency domain method, the phases of the different excitation frequencies do not play the same role as in heterodyned methods. TRIVE-FWM has the ability to probe cross peaks between vibrational modes that are widely separated in frequency.

This study uses the CS_2 ν_1 symmetric stretch at 656 cm^{-1}, the ν_3 antisymmetric stretch at 1520 cm^{-1}, and the $(\nu_1 + \nu_3)$ and $(\nu_1 + 2\nu_3)$ combination bands at 2170 and 3670 cm^{-1} as a model system[13] to explore the characteristics of TRIVE-FWM that were predicted in an earlier publication.[12] Two tunable and coherent infrared sources (frequencies ω_1 and ω_2) create three excitation pulses (frequencies ω_1, ω_2, $\omega_{2'}$) that generate four-wave mixing in the $\vec{k}_4 = \vec{k}_1 - \vec{k}_2 + \vec{k}_{2'}$ phase-matching direction. A monochromator measures the output beam intensity at ω_4 as a function of the ω_1 and ω_2 frequencies and the $\tau_{ij} = \tau_i - \tau_j$ temporal delays of the *i* and *j* input pulses. Figure 1 shows the 13 TRIVE coherence pathways that define the temporal evolution of the CS_2 molecular coherences. The pathway labeled TRIVE-Raman is important if ω_1 is tuned to a combination band and is negligible if the first transition involves a fundamental mode. The 13 pathways create material polarizations that interfere at the amplitude level to create the ω_4 output polarization. In TRIVE-FWM, appropriate selection of the frequencies of ω_1, ω_2, and $\omega_{2'}$, the two time delays between the three excitation beams, and the detection frequency, ω_4, controls the relative importance of different pathways and their interference effects. This control allows either the selection of a specific pathway or the choice of multiple pathways that can interfere at the amplitude level and allow coherent control of the relative intensities of features in a multidimensional spectrum.[13]

The TRIVE-FWM processes are related to pump−probe methods. TRIVE-FWM and two-color pump−probe experiments share the same coherence pathways,[8] but they also have important differences. Pump−probe experiments use a pump to create a population followed by a probe whose intensity measures the changes in population caused by the pump. The different coherence pathways interfere and result in probe beam intensity increases and decreases depending upon the relative contributions from the bleaching (analogous to pathways Iα, Iβ, IIIα, and IIIβ in Figure 1), stimulated emission (Vα and VIα), two-photon absorption (IIα, IIβ, IVα, and IVβ), and excited-state absorption (Vβ and VIβ) pathways.[14,15] Because pump−probe methods involve two interactions at the amplitude level in the pump step, the methods are dominated by pathways Vα, VIα, Vβ, and VIβ. TRIVE-FWM processes create a new coherent beam whose intensity is controlled by three multiplicative resonance enhancements. Instead of measuring the intensity changes of a probe beam, the TRIVE method measures the

* Corresponding author. E-mail: wright@chem.wisc.edu.

10.1021/jp046137j CCC: $27.50
Published on Web 11/16/2004

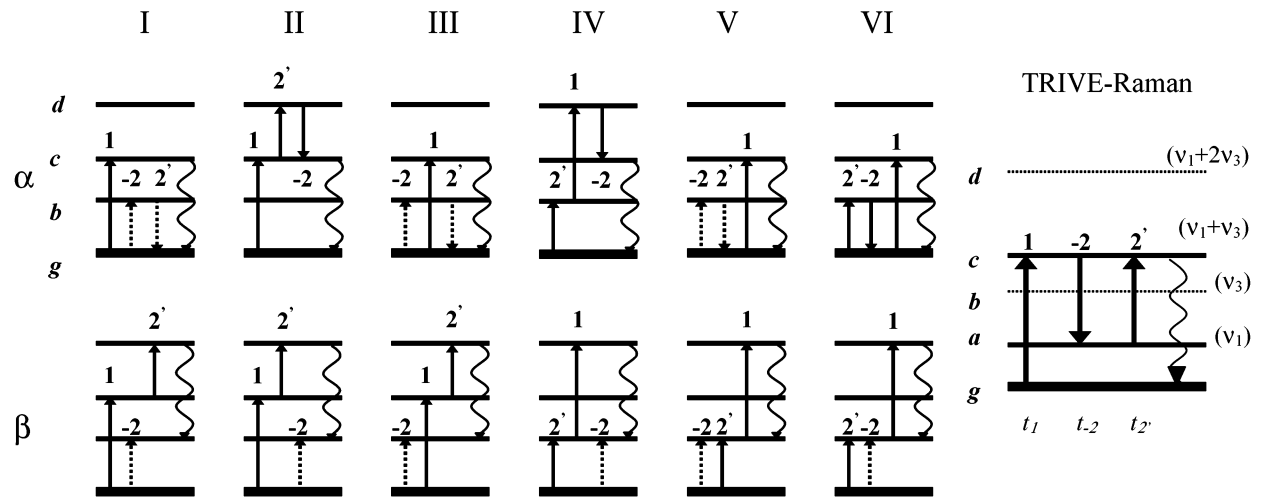

Figure 1. Twelve Lee−Albrecht diagrams for TRIVE-FWM. The *g, a, b, c,* and *d* letters designate the ground, ν_1, ν_3, $(\nu_1 + \nu_3)$ and $(\nu_1 + 2\nu_3)$ states, respectively. Levels *c* and *d* are combination bands and are shifted by the anharmonic coupling values ξ' and ξ, respectively. Solid lines represent ket-side transitions, dotted lines represent bra-side transitions, and the wavy line represents the radiated output. Processes in the top row (labeled α) involve even numbers of bra interactions, whereas processes in the bottom row (labeled β) involve odd numbers. If state *c* is not a combination band, then the TRIVE-Raman pathway is not present. The t_i represent the absolute time of the *i*th pulse.

intensity of a new beam created in the phase-matched direction. We show that appropriate selection of the excitation frequencies, time delays, and output frequency in TRIVE-FWM controls the interference between pathways. Because the excitation pulse widths in these experiments are close to the dephasing times (∼1−10 ps), one can use time delays to either enhance or attenuate one or several pathways, so the interference effects can coherently control the relative intensities of features in a multidimensional spectrum.

Theory

The nonlinear polarization responsible for creating the TRIVE-FWM output is related to the electric fields of the excitation pulses by the response function. We will assume the homogeneous limit for the work in this paper and use the Iα pathway as an example. The extension to the other pathways is summarized in Tables 1 and 2.[12,16,17] The nonlinear polarization is then given by the expression

$$\vec{P}^{(3)}_{1\alpha}(\vec{k}_{2'}, \vec{k}_2, \vec{k}_1, t) = N\int_0^\infty\int_0^\infty\int_0^\infty \{\vec{E}_{2'}(\vec{k}_{2'}, t - t_{2'})\} \times \{\vec{E}_2(\vec{k}_2, t - t_2 - t_{2'} + \tau_{2'2})\}\{\vec{E}_1(\vec{k}_1, t - t_1 - t_2 - t_{2'} + \tau_{21} + \tau_{2'2})\} \times S^{(3)}_{1\alpha}(t_3, t_2, t_1)\, dt_3\, dt_2\, dt_1 + c.c. \quad (1)$$

where the response function for the Iα pathway is

$$S^{(3)}_{1\alpha}(t_3, t_2, t_1) = \left(\frac{i}{\hbar}\right)^3 \mu_{go}\mu_{gb}\mu_{bg}\mu_{cg}\theta(t_{2'}) \times \exp[(-i\omega_{cg} - \Gamma_{cg})t_{2'}]\theta(t_2) \exp[(-i\omega_{cb} - \Gamma_{cb})t_2]\cdot\theta(t_1) \times \exp[(-i\omega_{cg} - \Gamma_{cg})t_1]\rho_{gg}(0) \quad (2)$$

Here, μ_{ij} and ω_{ij} are the moments and frequency of the $i-j$ transition, the $\theta(t)$ functions are Heaviside functions that enforce causality, and $\rho_{gg}(0)$ is the initial value of the ground-state density function. The dephasing rate between states *i* and *j* is $\Gamma_{ij} = (\Gamma_{ii} + \Gamma_{jj})/2 + \Gamma^*_{ij}$ where the diagonal dephasing rates, Γ_{ii} and Γ_{jj}, represent population relaxation of the *i* and *j* states and Γ^*_{ij} is the pure dephasing rate for the transition. If one of the states is a combination band, then the dephasing rates from different states are related, depending upon the correlation of the solvent-induced fluctuations in the frequencies of the two states. If state *c* is a combination band involving states *a* and *b*, then one can write $\Gamma^*_{cg} = \Gamma^*_{ag} + \Gamma^*_{bg} + 2\eta_{ab}\sqrt{\Gamma^*_{ag}\Gamma^*_{bg}}$, where η_{ab} is the correlation coefficient for the two levels.[16,17] We assume that the exciting electric fields, E_i, are Gaussian with the form $E_i^o \exp(-t^2/\sigma_i^2)$. The net nonlinear polarization requires summation over the contributions from all of the pathways diagrammed in Figure 1. Because the output intensity depends on the square of the electric field created by the nonlinear polarization, there will be cross terms between each of the pathways' contributions that define the observed interference effects.

For the experiments reported in this paper, two pulses have the same frequencies, so not all pathways can be fully resonant. The 2D spectra predicted in the steady-state limit for this two-color case have been previously described.[12] The magnitude and the real and imaginary parts of the resonant third-order susceptibility for each pathway are shown in Figures 2 and 3 as a function of the two excitation frequencies, ω_1 and ω_2. The triply resonant pathways have a single peak in the magnitude spectrum, whereas the doubly resonant pathways have two or three peaks, depending upon the number of coherence pairs that can be resonant under the conditions of the experiment.

Experimental Section

The experiments use a Ti:sapphire-pumped dual-OPA system that creates independently tunable 1-ps, 20-cm^{-1} fwhm, vertically polarized infrared pulses. The OPA ω_2 output is split to create the $\vec{k}_2$ and $\vec{k}_{2'}$ beams required for the $\vec{k}_4 = \vec{k}_1 - \vec{k}_2 + \vec{k}_{2'}$ phase-matching geometry previously described.[11] The output is isolated with an aperture and measured with a 0.3-m monochromator, a 2-cm^{-1} bandwidth, and a single-element cooled MCT detector tuned to ω_m. The sample consists of a 100-μm-thick 0.3 mol % CS_2/99.7% CH_2Cl_2 solution sandwiched between two 3-mm optically smooth CaF_2 windows. The ω_1 value is tuned near the $\nu_1 + \nu_3$ combination band at 2170 cm^{-1}, and the ω_2 value is tuned near the ν_3 fundamental at 1520 cm^{-1}. Note also that $(\omega_1 - \omega_2)$ is near the ν_1 fundamental at 660 cm^{-1}. The frequency accuracy is 2 cm^{-1}.

Results and Discussion

Because the pulses' temporal widths are similar to the dephasing times, the response function lies between the CW

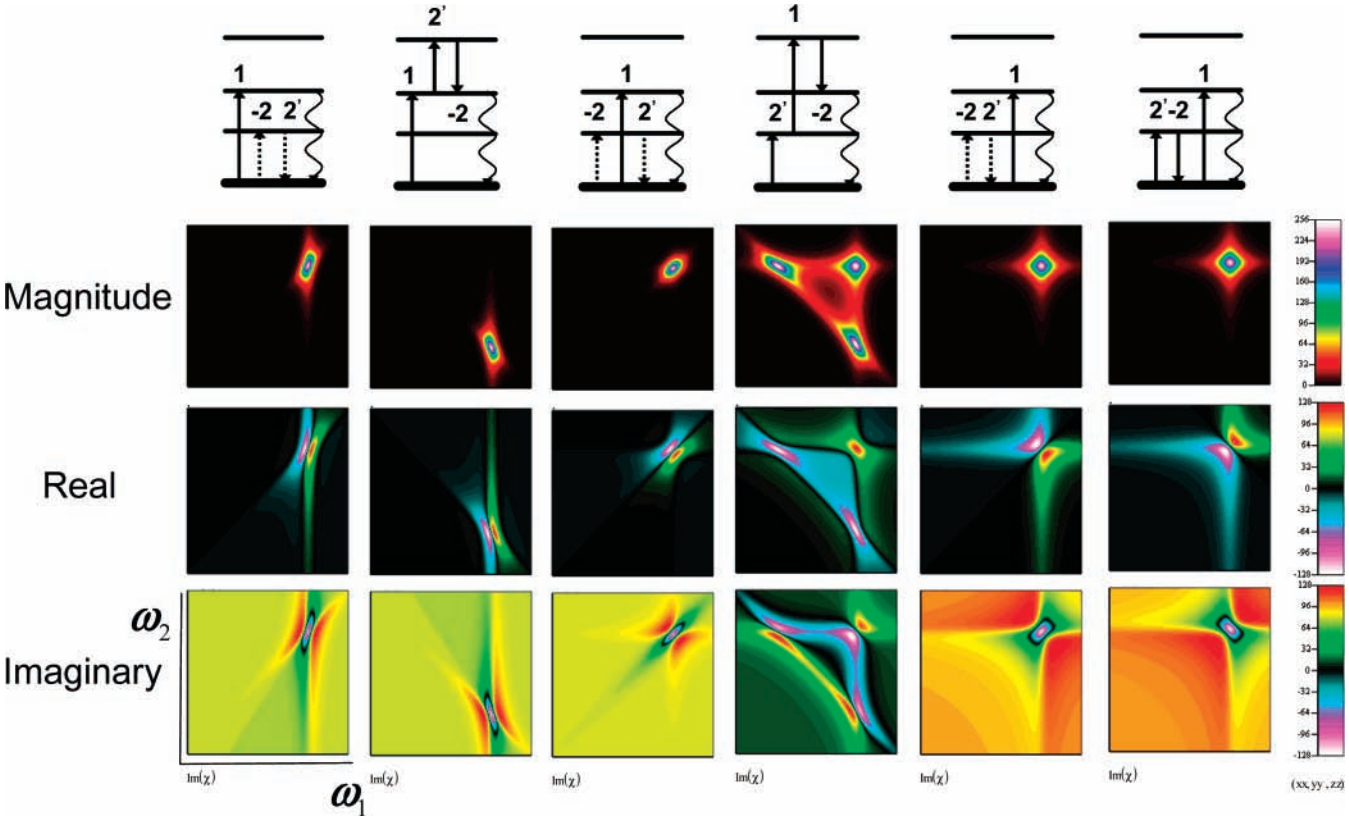

Figure 2. Magnitude and real and imaginary parts of the steady-state $\chi^{(3)}$ for the six α pathways in a two-color experiment where the intensity is measured as a function of ω_1 and ω_2.

TABLE 1: Form for *P*(*t*) for Different Pathways[a]

$P^{(3)}(t)$	pathways[1]
$N\int_0^\infty\int_0^\infty\int_0^\infty \vec{E}_{2'}(t-t_3)\vec{E}_2(t-t_2-t_3+\tau_{2'2})\vec{E}_1(t-t_1-t_2-t_3+\tau_{21}+\tau_{2'2})\, S^{(3)}(t_1,t_2,t_3)\, dt_3\, dt_2\, dt_1$	Iα, Iβ
$N\int_0^\infty\int_0^\infty\int_0^\infty \vec{E}_2(t-t_3+\tau_{2'2})\vec{E}_{2'}(t-t_2-t_3)\vec{E}_1(t-t_1-t_2-t_3+\tau_{21}+\tau_{2'2})\, S^{(3)}(t_1,t_2,t_3)\, dt_3\, dt_2\, dt_1$	IIα, IIβ
$N\int_0^\infty\int_0^\infty\int_0^\infty \vec{E}_{2'}(t-t_3)\vec{E}_1(t-t_2-t_3+\tau_{21}+\tau_{2'2})\vec{E}_2(t-t_1-t_2-t_3+\tau_{2'2})S^{(3)}(t_1,t_2,t_3)\, dt_3\, dt_2\, dt_1$	IIIα, IIIβ
$N\int_0^\infty\int_0^\infty\int_0^\infty \vec{E}_2(t-t_3+\tau_{2'2})\vec{E}_1(t-t_2-t_3+\tau_{21}+\tau_{2'2})\vec{E}_{2'}(t-t_1-t_2-t_3)\, S^{(3)}(t_1,t_2,t_3)\, dt_3\, dt_2\, dt_1$	IVα, IVβ
$N\int_0^\infty\int_0^\infty\int_0^\infty \vec{E}_1(t-t_3+\tau_{21}+\tau_{2'2})\vec{E}_{2'}(t-t_2-t_3)\vec{E}_2(t-t_1-t_2-t_3+\tau_{2'2})\, S^{(3)}(t_1,t_2,t_3)\, dt_3\, dt_2\, dt_1$	Vα, Vβ
$N\int_0^\infty\int_0^\infty\int_0^\infty \vec{E}_1(t-t_3+\tau_{21}+\tau_{2'2})\vec{E}_2(t-t_2-t_3+\tau_{2'2})\vec{E}_{2'}(t-t_1-t_2-t_3)\, S^{(3)}(t_1,t_2,t_3)\, dt_3\, dt_2\, dt_1$	VIα, VIβ

[1]TRIVE-Raman has the same function as TRIVE Iα when $\omega_1 > \omega_2$ or TRIVE IIIα when $\omega_2 > \omega_1$

[a] Wavevector arguments are not included. Adding the complex conjugate is assumed for all forms.

TABLE 2: Functions *S*(*t*) for Each Pathway

Iα	$(i/\hbar)^3\mu_{gc}\mu_{gb}\mu_{bg}\mu_{cg}\theta(t_3)e^{-i\omega_{cg}t_3}e^{-\Gamma_{cg}t_3}\theta(t_2)e^{-i\omega_{cb}t_2}e^{-\Gamma_{cb}t_2}\theta(t_1)e^{-i\omega_{cg}t_1}e^{-\Gamma_{cg}t_1}\rho(0)$
Iβ	$-(i/\hbar)^3\mu_{bd}\mu_{dc}\mu_{bg}\mu_{cg}\theta(t_3)e^{-i\omega_{dg}t_3}e^{-\Gamma_{db}t_3}\theta(t_2)e^{-i\omega_{cb}t_2}e^{-\Gamma_{cb}t_2}\theta(t_1)e^{-i\omega_{cg}t_1}e^{-\Gamma_{cg}t_1}\rho(0)$
IIα	$(i/\hbar)^3\mu_{gc}\mu_{cd}\mu_{dc}\mu_{cg}\theta(t_3)e^{-i\omega_{cg}t_3}e^{-\Gamma_{cg}t_3}\theta(t_2)e^{-i\omega_{dg}t_2}e^{-\Gamma_{dg}t_2}\theta(t_1)e^{-i\omega_{cg}t_1}e^{-\Gamma_{cg}t_1}\rho(0)$
IIβ	$-(i/\hbar)^3\mu_{bd}\mu_{bg}\mu_{dc}\mu_{cg}\theta(t_3)e^{-i\omega_{dg}t_3}e^{-\Gamma_{db}t_3}\theta(t_2)e^{-i\omega_{dg}t_2}e^{-\Gamma_{dg}t_2}\theta(t_1)e^{-i\omega_{cg}t_1}e^{-\Gamma_{cg}t_1}\rho(0)$
IIIIα	$(i/\hbar)^3\mu_{gc}\mu_{gb}\mu_{cg}\mu_{bg}\theta(t_3)e^{-i\omega_{cg}t_3}e^{-\Gamma_{cg}t_3}\theta(t_2)e^{-i\omega_{cb}t_2}e^{-\Gamma_{cb}t_2}\theta(t_1)e^{-i\omega_{gb}t_1}e^{-\Gamma_{gb}t_1}\rho(0)$
IIIβ	$-(i/\hbar)^3\mu_{bd}\mu_{dc}\mu_{cg}\mu_{bg}\theta(t_3)e^{-i\omega_{dg}t_3}e^{-\Gamma_{db}t_3}\theta(t_2)e^{-i\omega_{cb}t_2}e^{-\Gamma_{cb}t_2}\theta(t_1)e^{-i\omega_{gb}t_1}e^{-\Gamma_{gb}t_1}\rho(0)$
IVα	$(i/\hbar)^3\mu_{gc}\mu_{cd}\mu_{dc}\mu_{bg}\theta(t_3)e^{-i\omega_{cg}t_3}e^{-\Gamma_{cg}t_3}\theta(t_2)e^{-i\omega_{dg}t_2}e^{-\Gamma_{dg}t_2}\theta(t_1)e^{-i\omega_{bg}t_1}e^{-\Gamma_{bg}t_1}\rho(0)$
IVβ	$-(i/\hbar)^3\mu_{bd}\mu_{bg}\mu_{db}\mu_{bg}\theta(t_3)e^{-i\omega_{dg}t_3}e^{-\Gamma_{db}t_3}\theta(t_2)e^{-i\omega_{dg}t_2}e^{-\Gamma_{dg}t_2}\theta(t_1)e^{-i\omega_{bg}t_1}e^{-\Gamma_{bg}t_1}\rho(0)$
Vα	$(i/\hbar)^3\mu_{gc}\mu_{cg}\mu_{gb}\mu_{bg}\theta(t_3)e^{-i\omega_{cg}t_3}e^{-\Gamma_{cg}t_3}\theta(t_2)e^{-\Gamma_{gg}t_2}\theta(t_1)e^{-i\omega_{gb}t_1}e^{-\Gamma_{gb}t_1}\rho(0)$
Vβ	$-(i/\hbar)^3\mu_{bd}\mu_{db}\mu_{bg}\mu_{bg}\theta(t_3)e^{-i\omega_{db}t_3}e^{-\Gamma_{db}t_3}\theta(t_2)e^{-\Gamma_{bb}t_2}\theta(t_1)e^{-i\omega_{gb}t_1}e^{-\Gamma_{gb}t_1}\rho(0)$
VIα	$(i/\hbar)^3\mu_{gc}\mu_{cg}\mu_{gb}\mu_{bg}\theta(t_3)e^{-i\omega_{cg}t_3}e^{-\Gamma_{cg}t_3}\theta(t_2)e^{-\Gamma_{gg}t_2}\theta(t_1)e^{-i\omega_{bg}t_1}e^{-\Gamma_{bg}t_1}\rho(0)$
VIβ	$-(i/\hbar)^3\mu_{bd}\mu_{db}\mu_{bg}\mu_{bg}\theta(t_3)e^{-i\omega_{db}t_3}e^{-\Gamma_{db}t_3}\theta(t_2)e^{-\Gamma_{bb}t_2}\theta(t_1)e^{-i\omega_{bg}t_1}e^{-\Gamma_{bg}t_1}\rho(0)$
TRIVE-Raman $\omega_1 > \omega_2$	$(i/\hbar)^3\mu_{gc}\mu_{ca}\mu_{ac}\mu_{cg}\theta(t_3)e^{-i\omega_{cg}t_3}e^{-\Gamma_{cg}t_3}\theta(t_2)e^{-i\omega_{ag}t_2}e^{-\Gamma_{ag}t_2}\theta(t_1)e^{-i\omega_{cg}t_1}e^{-\Gamma_{cg}t_1}\rho(0)$
TRIVE-Raman $\omega_2 > \omega_1$	$(i/\hbar)^3\mu_{ac}\mu_{cg}\mu_{ac}\mu_{cg}\theta(t_3)e^{-i\omega_{ca}t_3}e^{-\Gamma_{ca}t_3}\theta(t_2)e^{-i\omega_{ga}t_2}e^{-\Gamma_{ag}t_2}\theta(t_1)e^{-i\omega_{gc}t_1}e^{-\Gamma_{cg}t_1}\rho(0)$

and impulsive limits.[4,18] The output frequency can differ in each limit. The CW limit corresponds to a forced oscillator model where the output coherence frequency is defined by the linear combination of the excitation field frequencies. Because the excitation line width is narrow and lies within the bandwidth of the molecular transition, the multidimensional spectrum is

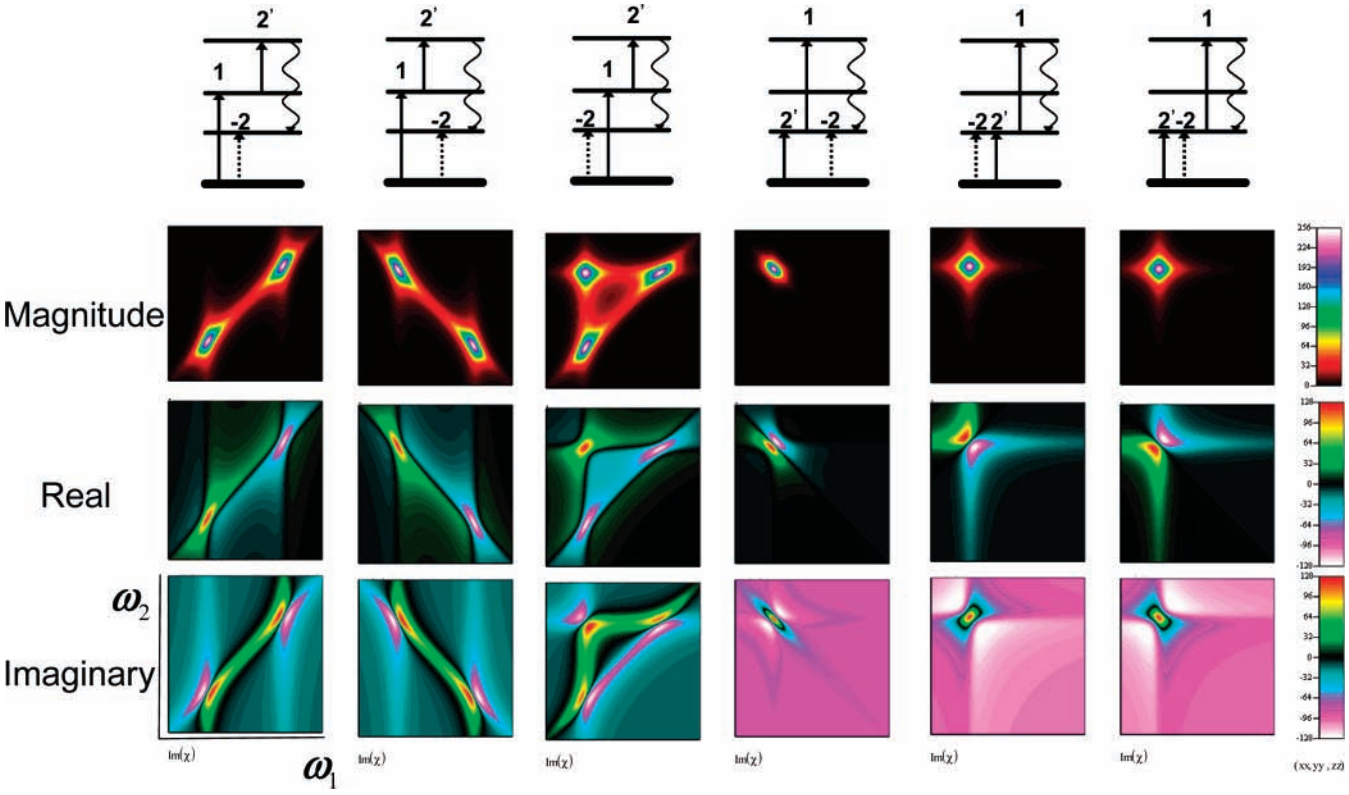

Figure 3. Magnitude and real and imaginary parts of the steady-state $\chi^{(3)}$ for the six β pathways in a two-color experiment where the intensity is measured as a function of ω_1 and ω_2.

TABLE 3: Summary of the Peaks Expected for a Two-Color TRIVE Experiment in Dilute Carbon Disulfide for Each Pathway in Figure 1[a]

			driven oscillator			free-induction decay		
pathway	enhancements	resonant coherences	ω_1 (cm^{-1})	ω_2 (cm^{-1})	ω_m (cm^{-1})	ω_1 (cm^{-1})	ω_2 (cm^{-1})	ω_m (cm^{-1})
Iα	triply enhanced	*cg, cb, cg*	2170	1520	2170	2170	1520	2170
IIα	triply enhanced	*cg, dg, cg*	2170	1500	2170	2170	1500	2170
IIIα	triply enhanced	*gb, cb, cg*	2170	1520	2170	2170	1520	2170
IVα	doubly enhanced	*bg, dg*	2150	1520	2150	2150	1520	2170
	doubly enhanced	*bg, cg*	2170	1520	2170	2170	1520	2170
	doubly enhanced	*dg, cg*	2170	1500	2170	2170	1500	2170
Vα	triply enhanced	*gb, gg, cg*	2170	1520	2170	2170	1520	2170
VIα	triply enhanced	*bg, gg, cg*	2170	1520	2170	2170	1520	2170
Iβ	doubly enhanced	*cg,cb*	2170	1520	2170	2170	1520	2150
	doubly enhanced	*cb, db*	2150	1500	2150	2150	1500	2150
IIβ	doubly enhanced	*cg, dg*	2170	1500	2170	2170	1500	2150
	doubly enhanced	*dg, db*	2150	1520	2150	2150	1520	2150
IIIβ	doubly enhanced	*gb, cb*	2170	1520	2170	2170	1520	2150
	doubly enhanced	*gb, db*	2150	1520	2150	2150	1520	2150
	doubly enhanced	*cb, db*	2150	1500	2150	2150	1500	2150
IVβ	triply enhanced	*bg, dg, db*	2150	1520	2150	2150	1520	2150
Vβ	triply enhanced	*gb, dg, db*	2150	1520	2150	2150	1520	2150
VIβ	triply enhanced	*bg, bb, db*	2150	1520	2150	2150	1520	2150
TRIVE Raman	triply enhanced	*cg, ag, cg*	2170	1510	2170	2170	1510	2170

[a] Letters in the resonant coherences label the two vibrational states referenced in Figure 1 for the two-color experiment.

recorded in the frequency domain. The impulsive limit corresponds to the free-induction decay model where the output coherence radiates at its natural frequency. Because most of the excitation energy lies outside the bandwidth of the molecular transition, the multidimensional spectrum is recorded in the time domain. Simulations of our experiments show that the output signal has important contributions from both the forced oscillator and the free-induction decay.

Because our experiments have only two tunable frequencies (labeled ω_1 and ω_2), pathways Iβ, IIβ, IIIβ, and IVα may allow only two resonances if the frequency differences exceed the bandwidth of ω_2 and $\omega_{2'}$.[12] The remaining eight pathways are triply resonant. The eight fully resonant diagrams in Figure 1 predict peaks at three positions—(ω_1, ω_2, ω_m) = (2170, 1520, 2170), (2170, 1500, 2170), and (2150, 1520, 2150) cm^{-1}. These positions correspond to the ground-state transitions to ν_3 and $\nu_1 + \nu_3$ at 1520 and 2170 cm^{-1}, respectively, and the excited-state transitions $\nu_1 + \nu_3 \rightarrow \nu_1 + 2\nu_3$ and $\nu_3 \rightarrow \nu_1 + 2\nu_3$ that are anharmonically shifted by ξ to 1500 and 2150 cm^{-1}, respectively. In addition, there is a ninth fully resonant peak from the

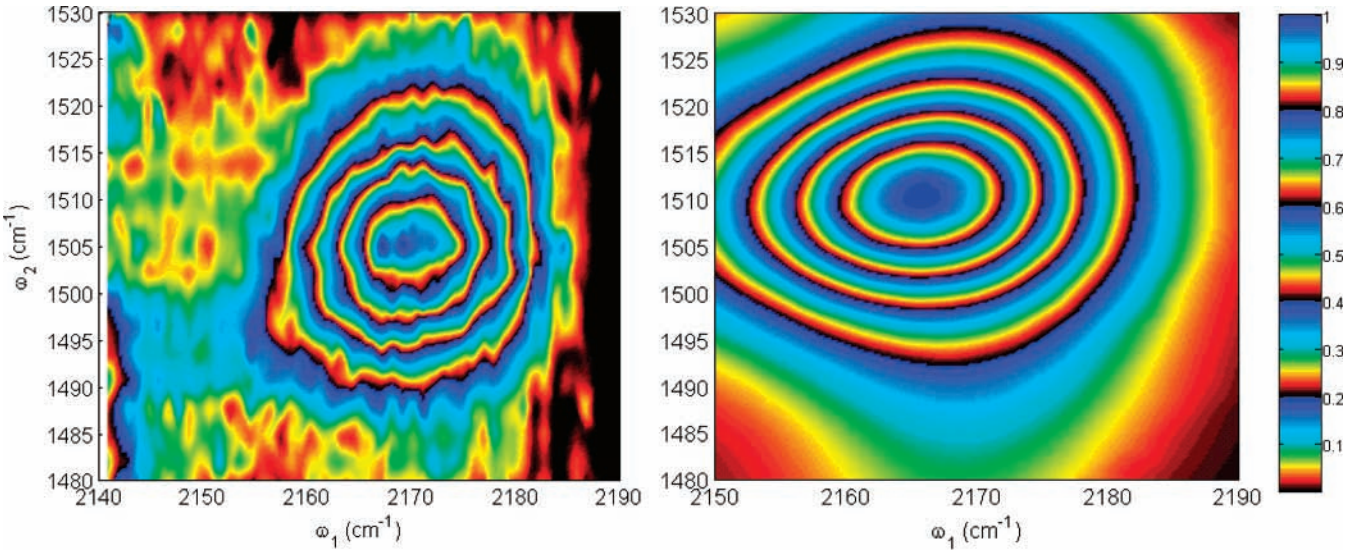

Figure 4. Two-dimensional TRIVE spectra where all output frequencies are monitored as a function of the two excitation frequencies. There is no time delay between pulses. (Left) experimental; (right) simulation.

TRIVE-Raman process (Figure 1) at (2170, 1510, 2170) cm^{-1}, where the 1510-cm^{-1} position is associated with the $\nu_1 + \nu_3 \rightarrow \nu_3$ transition that is anharmonically shifted by ξ' from the ground-state transition. There are two or three possible peak positions for the four diagrams in Figure 1 that are not fully resonant. These peak positions depend on the excitation frequency bandwidths of ω_1 and ω_2 and the size of the forced oscillator or free-induction decay contributions. All of the possible peak positions are summarized in Table 3 and discussed more fully elsewhere.[12]

Figure 4a shows the TRIVE-FWM 2D ω_1, ω_2 dependence where no monochromator was used to select the output frequency and the three excitation beams were temporally overlapped. Only one discernible peak appears at the (ω_1, ω_2) = (2170, 1506) cm^{-1} position despite the fact that all of the pathways in Figure 1 should contribute. The effects of these pathways can be simulated. The spectrum in Figure 4b is a simulation using the response functions in the homogeneously broadened limit described earlier. The simulations used 0.8-ps-intensity fwhm Gaussian pulses with the measured experimental delays defined in the Figures, line widths from IR, Raman, and DOVE spectra, and an anharmonicity, $\xi = 19$ cm^{-1}, for the excited-state transitions.[12] A scaling factor of $\sqrt{2}$ was used to calculate the excited-state transition dipoles from the ground-state dipoles.[6] These values were not adjusted to fit the spectra. The simulation shows that although the 13 different pathways in Figure 1 produce peaks at three different positions the net contribution from all of them merges the three peaks into a single symmetrical peak at an intermediate spectral position. The simulations predict the correct position of the peak for ω_2, but the peak is shifted to significantly lower values of ω_1 and its shape is different from that observed. The values for the simulation are summarized in Table 4.

The participation of the different pathways becomes clearer if the experimental variables are chosen to discriminate between the pathways. Figure 5 contains examples of how using a monochromator with frequency ω_m can spectrally resolve the output frequency and provide discrimination. The Figure has a series of related 2D TRIVE spectra that show the (ω_m, ω_1) dependence for different values of ω_2 and pulse time delays. In the top row of spectra, the three excitation pulses are temporally overlapped as they were in Figure 4. Note that a second weak diagonal peak appears and becomes stronger as ω_2 moves

TABLE 4: Summary of Parameters Used for the Combination Band TRIVE CS_2 Simulations, in Wavenumbers except as Indicated

resonance frequencies:	ω_{cg}	2169 cm^{-1}
	ω_{bg}	1520 cm^{-1}
	ω_{dg}	3669 cm^{-1}
	ω_{ag}	656 cm^{-1}
population relaxation dephasing parameters:	$(\Gamma_{cc} + \Gamma_{gg})/2$	1.3 cm^{-1}
	$(\Gamma_{bb} + \Gamma_{gg})/2$	0.8 cm^{-1}
	$(\Gamma_{dd} + \Gamma_{gg})/2$	2 cm^{-1}
	$(\Gamma_{aa} + \Gamma_{gg})/2$	0 cm^{-1}
	$(\Gamma_{cc} + \Gamma_{bb})2$	2 cm^{-1}
	$(\Gamma_{dd} + \Gamma_{bb})/2$	3 cm^{-1}
	$\Gamma_{gg} = \Gamma_{bb}$	1 cm^{-1}
pure dephasing parameters:		Γ^*_{bg}1.7 cm^{-1}
		Γ^*_{ag}0.18 cm^{-1}
	η_{ab}	1
electric field parameters:	$\sigma_1 = \sigma_2 = \sigma_2$'	0.7 ps

toward 1520 cm^{-1}. When $\omega_2 = 1520$ cm^{-1} and the pulses are temporally overlapped, pathways Iα, IIIα, Vα, and VIα create a triply resonant peak at (ω_m, ω_1) = (2170, 2170) cm^{-1} that corresponds to the strongest peak in the spectra. In addition, pathways IVβ, Vβ, and VIβ create a triply resonant peak at (ω_m, ω_1) = (2150, 2150) cm^{-1} that correspond to the weaker diagonal peak. There are also less important contributions from the other pathways. For example, the IVα, Iβ, IIβ, and IIIβ pathways that are not fully resonant could produce peaks at either (ω_m, ω_1) = (2150, 2150) cm^{-1} or (2170, 2170) cm^{-1} or on the diagonal between these two positions if the majority of the signal is produced by the forced oscillator component. Any free-induction decay component would be observed directly at (2150, 2150) cm^{-1} for the IIβ and IIIβ paths, (2150,2170) cm^{-1} for the Iβ, IIβ, and IIIβ paths, and (2170, 2170) cm^{-1} and (2170, 2150) cm^{-1} for the IVα path. Pathway IIα should contribute negligibly in this spectrum because the fixed value of $\omega_2 = 1520$ cm^{-1} prevents it from achieving multiple vibrational resonance.

The observed spectrum with $\omega_2 = 1520$ cm^{-1} is consistent with the contributions from the eight fully resonant contributions because it shows two major peaks along the main diagonal. There is also an off-diagonal feature at (ω_m, ω_1) = (2150, 2170) cm^{-1} that cannot be fully resonant and cannot be from the forced

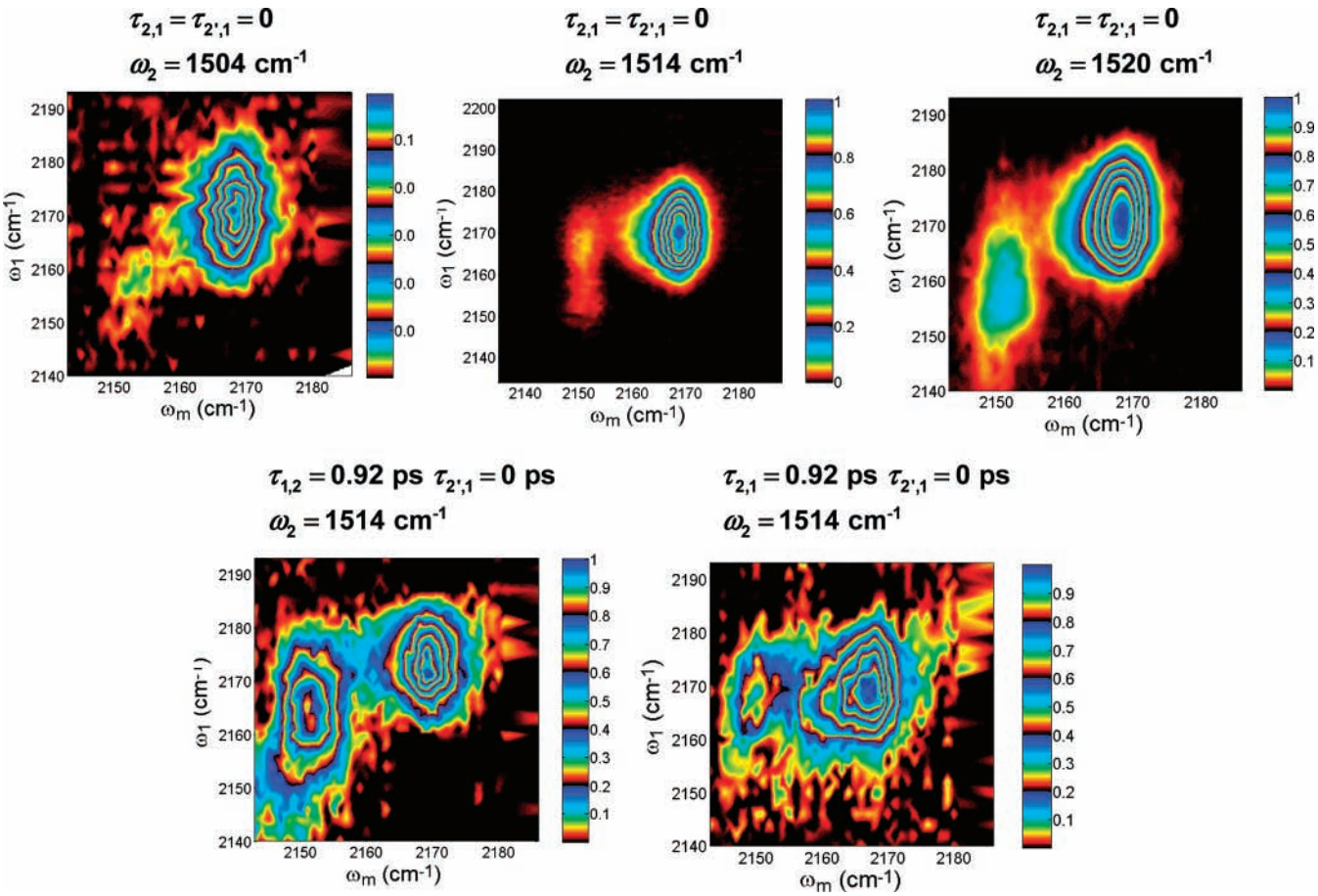

Figure 5. Two-dimensional TRIVE spectra where the pulse delays and ω_2 value are indicated and the ω_1 and the monochromator frequencies are changed.

oscillator component. The peak becomes stronger when ω_2 is between 1504 and 1520 cm^{-1}. It can arise only from free-induction decay terms in the less resonant paths, particularly the Iβ, IIβ, and IIIβ paths. These pathways are enhanced for the intermediate values of ω_2 because there is greater spectral overlap with the two resonances involving ω_2. The IVα path would produce a peak at (ω_m, ω_1) = (2170, 2150) cm^{-1} from the free-induction decay component of the signal, but it is either not observed or is suppressed by the fully resonant terms at (2170, 2170) cm^{-1}. The observation of a free-induction decay peak from the Iβ, IIβ, and IIIβ processes indicates that the monochromator could provide a significant increase in discrimination between α and β pathways for this dilute CS_2 system.

The bottom spectra in Figure 5 show the effects of introducing time delays. If the ω_1 pulse follows the ω_2 and ω_2' pulses (see the spectrum with τ_{12} = 0.92 ps), then the fully resonant contributions from the Vα,β and VIα,β pathways are enhanced. These pathways are responsible for the two diagonal peaks. If the ω_1 precedes the ω_2 and ω_2' pulses (see the spectrum with τ_{21}= 0.92 ps), then the contributions from the Iα,β and IIα,β pathways are enhanced. The Iα and IIα pathways are triply resonant and are responsible for the majority of the strong diagonal peak. The free-induction decay from the less resonant Iβ and IIβ pathways produces the off-diagonal peak in the Figure.

The changes in the relative intensity of the different spectral features in Figure 5 show that the selection of a monochromator frequency and pulse time delays introduces discrimination between the pathways contributing to the overall signal. Figures 6 and 7 show that appropriate choices of these parameters can provide sufficient discrimination to observe a single path. Figure 6 shows the spectra where the monochromator frequency selects for the α pathways, and Figure 7 shows the spectra where the monochromator frequency selects for the β pathways. In each Figure, individual pathways are represented by single columns that correspond to the chosen time delays. Each column contains (1) the experimental conditions that select a specific pathway, (2) a diagram of the selected pathway, (3) the experimental (ω_1, ω_2) spectrum, and (4) a simulated spectrum using the values in Table 4.

One can see that the position of the peak changes depending upon which pathway is enhanced by the selection of delays and monochromator position. These variables are summarized in the Figure. All of the triply resonant pathways have peaks at or close to the positions expected from the resonances. The doubly resonant peaks are not at defined positions in Figures 6 and 7 because Table 3 shows that there are two or three sets of resonant states that can provide double resonances that interfere and shift the expected peak positions.[12] The simulations show how the different double resonances and the interfering pathways are predicted to interfere and generate the observed peak. One can see that the simulations model the peak positions quite well. The peaks generally appear at intermediate positions between the two or three possible peak positions in Table 3 for the doubly vibrationally enhanced pathways. In each case, the interference between pathways is constructive, so one sees a single peak instead of two or three separate peaks.

The simulations also include the contributions from pathways other than the one optimized by the selection of temporal delay

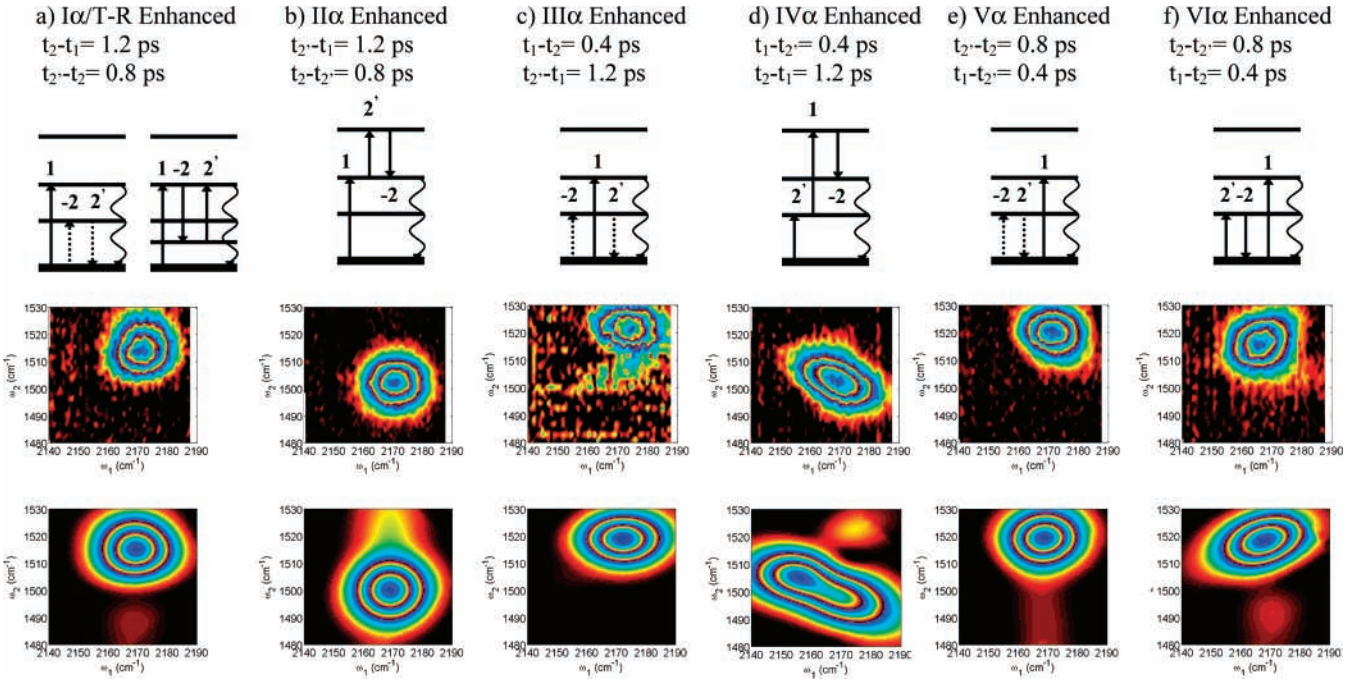

Figure 6. Spectra with temporal and spectral discrimination set to enhance specific TRIVE pathways. $\omega_m = 2168\ cm^{-1}$.

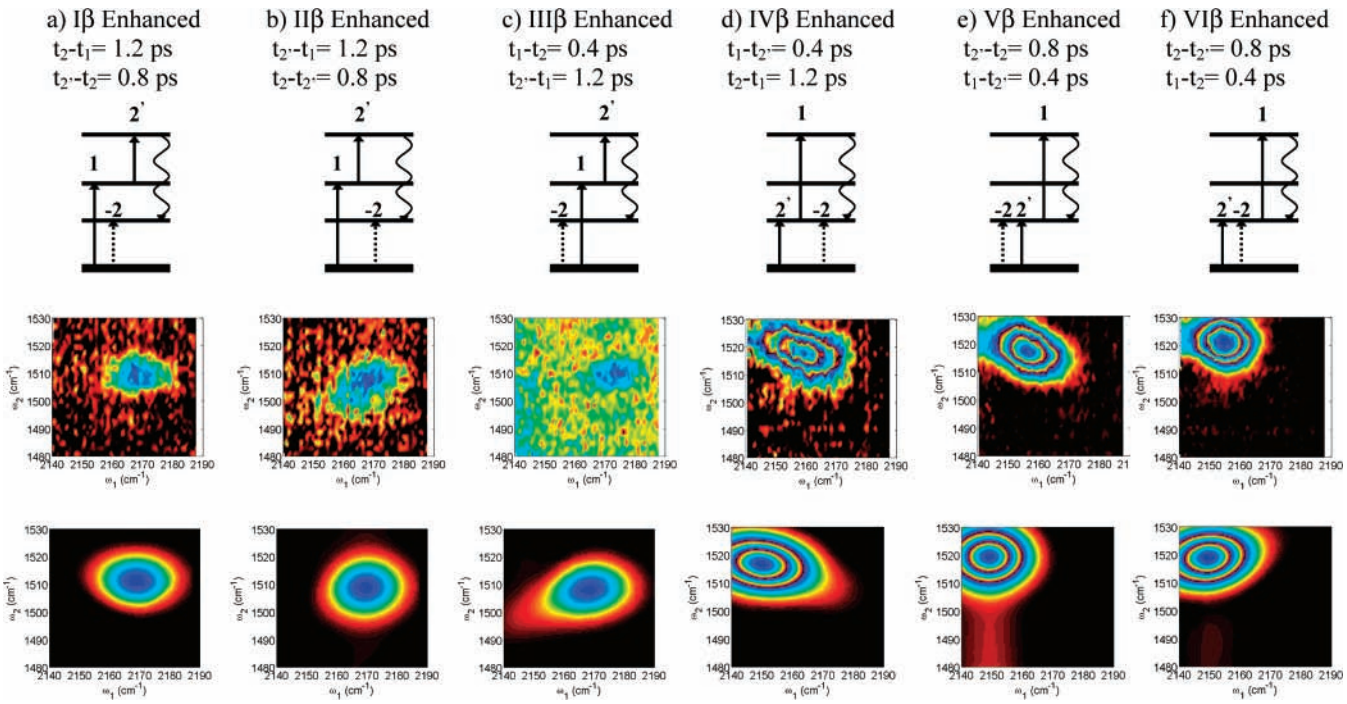

Figure 7. Spectra with temporal and spectral discrimination set to enhance specific TRIVE pathways. $\omega_m = 2149\ cm^{-1}$.

and monochromator position. The discrimination between pathways depends on the delay time relative to the pulse widths. The spectra with 400-fs delays have the least discrimination between pathways, and these spectra contain important contributions from other pathways. The spectrum for the VIα pathway has important contributions from the IVα pathway because of the small delay between the ω_1 and ω_2 beams, so the peak is shifted to lower ω_1 and ω_2 values. Similarly, the VIβ pathway spectrum has important contributions from the IVβ pathway, but in this case, the peaks expected from each pathway are identical and no shifting occurs in the peak position. Similarly, the IIIα pathway spectrum has important contributions from the Iα pathway that do not shift the expected peak position, the Vα pathway spectrum has important contributions from the IIIα pathway that do not shift the expected peak position, the IIIβ pathway spectrum has important contributions from the Iβ pathway that shift the position, the IVβ pathway spectrum has important contributions from the IIβ pathway that shift the peak frequency to lower ω_2 values, and the Vβ pathway spectrum has important contributions from the IVβ pathway that do not shift its peak position. In each of these examples, the peak position is adequately reproduced by the simulations.

There are differences between the observed spectra and the simulations. The simulations predict that the IVα pathway is shifted to a significantly different position than that observed. This case involves the most interfering processes because the

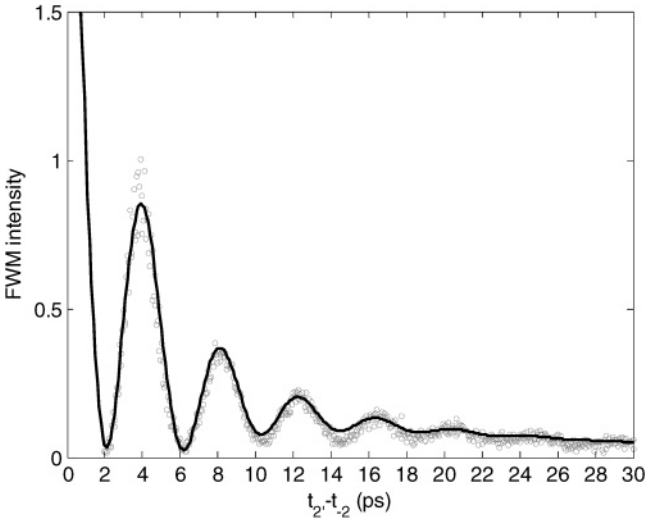

Figure 8. Coherent beating between Iα and TRIVE-Raman pathways. Gray dots are data, and the solid line is fit. The data show the intensity of the peak at $(\omega_1, \omega_2, \omega_m) = (2172, 1520, 2172)$ cm^{-1} for time delays where $t_2 - t_1 \approx 0$ ps and $t_{2'} - t_2$ is varied.

IVα pathway itself involves three different sets of doubly resonant states and significant contributions from the triply resonant IIα pathway. In addition, the simulations for the IIα and IVα pathways predict an additional feature that is not observed in the data. The simulations show that small changes in the simulation parameters can cause substantial differences in the simulated spectra. The observed differences are attributed to inaccuracies in the simulation parameters that define the relative contributions from the different processes.

The spectrum of the Iα pathway is interesting because the pulse sequence 1, −2, 2′ and monochromator setting of 2168 cm^{-1} required to enhance the Iα pathway also enhance the TRIVE-Raman pathway. The peak appears at $(\omega_1, \omega_2) = (2171, 1515)$ cm^{-1}, which is midway between the expected peaks at (2170, 1520) and (2170, 1510) from the respective Iα and TRIVE-Raman paths. As explained in the discussion of Figure 4b, there is also some contribution from the Iβ pathway because it also can produce an output at the monochromator frequency.

Note that none of these peak positions match that seen in Figure 4a (where many pathways are simultaneously probed) because of the constructive and destructive quantum interference between the pathways. Depending on the relative separation of the peaks, constructive interference can prevent the observation of separate peaks, so a single peak appears in an intermediate position. Such a behavior is seen in Figure 4a where a single peak appears at a shifted intermediate position. Shifting results from the complex interference between the pathways responsible for the (2170, 1520)- and (2170, 1500)-cm^{-1} peaks. Similarly, the (2150, 1520)-cm^{-1} peak does not appear because of destructive interference. The conditions that isolate a particular pathway remove the interference from the other pathways, so one can observe the individual contributions. This example shows that one can employ temporal discrimination and output wavelength selection to dissect the contributions from individual pathways to the net response.

The interference between different pathways can also be used for coherent control of the relative intensities in these 2D spectra.[13,19−23] Figure 8 shows the results of an experiment that monitors the intensity of the peak at $(\omega_1, \omega_2, \omega_m) = (2172, 1520, 2172)$ cm^{-1} for time delays where $t_2 - t_1 \approx 0$ ps and $t_{2'} - t_2$ is varied. Under these conditions, the Iα, IIIα, and TRIVE-Raman pathways should contribute equally, and because they involve different coherences, they will experience quantum beating. After the first two interactions with ω_1 and ω_2, the Iα and IIIα pathways both produce a ρ_{cb} coherence involving the $c = (\nu_1 + \nu_3)$ and $b = \nu_3$ states, whereas the TRIVE-Raman pathway produces a ρ_{ag} coherence involving the $a = \nu_1$ and the ground state. The Figure shows that the character of the interference changes as a function of the $t_{2'} - t_2$ time delay, so the intensity of this peak can be enhanced or depressed. The beating between the three pathways can be described quantitatively by the expression

$$I(t) \propto |2e^{-\Gamma_{cb}t}e^{-i\omega_{cb}t} + e^{-\Gamma_{ag}t}e^{-i\omega_{ag}t}|^2$$

where ω_{ij} and Γ_{ij} are the frequencies and dephasing rates of the ij coherence. The factor of 2 comes from the presence of both Iα and IIIα processes, which have the same intermediate coherence, cb. The frequencies of the two coherences differ by $\xi' = 8.1$ cm^{-1}, and they therefore beat with a 4-ps period, in agreement with that from the spectra and TRIVE-Raman incorporation into the fits in Figures 4−7. Fitting of the temporal dependence results in values of $\Gamma_{cb} = 1.1$ cm^{-1} and $\Gamma_{ag} = 0.15$ cm^{-1}. Similar beating is observed in DOVE experiments in the same material except the interference between the pathways has the opposite sign from the TRIVE experiments reported here.[13] With zero delays, the pathways in DOVE destructively interfered so the intensity was a minimum, whereas the interfering TRIVE pathways constructively interfere so the intensity was a maximum. However, the coherences that are probed in the two experiments are the same, and the measured dephasing rates agree between the experiments.[13] The value of ξ' and Γ_{ag} are nearly equal to the values expected from linear-IR and Raman spectra.

Conclusions

TRIVE-FWM's importance arises because it allows one to perform fully resonant coherent multidimensional experiments on modes that are well separated in frequency. It is complementary to doubly vibrationally enhanced (DOVE) FWM, which also has this capability.[5,24−26] TRIVE methods are fully vibrationally resonant; therefore, one expects larger nonlinear susceptibilities than obtained with DOVE methods. Cross peaks appear in both methods, but they depend on different effects. In TRIVE methods, the cross peaks appear because mode coupling changes the transition frequency, transition moments, or dephasing rates so that the destructive interference between different pathways is incomplete. In DOVE methods, at least one of the transitions in the FWM must involve a combination band transition that is forbidden in the absence of mode coupling. Like all of the multidimensional methods, TRIVE-FWM allows one to observe the states and dephasing processes of the double vibrational coherences that are not accessible by traditional methods.

Though this experiment provides a method for enhancing a particular pathway, it is important to recognize that the degree of discrimination between pathways is strongly influenced by both the material's line widths, anharmonicities, and broadening mechanisms and the input pulses' widths and delay times. The optimum pulse width depends on the dephasing time of the coherences. If the pulse width is much longer than the dephasing times, then the resolution will be limited by the dephasing time but temporal selection of different pathways is not possible. If the pulse width is much shorter than the dephasing times, then the resolution will be limited by the spectral width of the pulses but excellent temporal selection is

possible. Pulse widths that are similar to the dephasing times optimize both goals, and simulations can assist in an understanding of the relative contributions from different pathways and the resulting interferences.

Acknowledgment. We gratefully acknowledge the contributions of Stuart Burke and Adrian Williams to this research. This work was supported by the Chemistry Program of the National Science Foundation under grant CHE-0130947.

References and Notes

(1) Scheurer, C.; Mukamel, S. *J. Chem. Phys.* **2001**, *115*, 4989.
(2) Scheurer, C.; Mukamel, S. *Bull. Chem. Soc. Jpn.* **2002**, *75*, 989.
(3) Scheurer, C.; Mukamel, S. *J. Chem. Phys.* **2002**, *116*, 6803.
(4) Mukamel, S. *Annu. Rev. Phys. Chem.* **2000**, *51*, 691.
(5) Wright, J. C. *Int. Rev. Phys. Chem.* **2002**, *21*, 185.
(6) Asplund, M. C.; Zanni, M. T.; Hochstrasser, R. M. *Proc. Natl. Acad. Sci. U.S.A.* **2000**, *97*, 8219.
(7) Zanni, M. T.; Asplund, M. C.; Hochstrasser, R. M. *J. Chem. Phys.* **2001**, *114*, 4579.
(8) Rubtsov, I. V.; Wang, J. P.; Hochstrasser, R. M. *J. Phys. Chem. A* **2003**, *107*, 3384.
(9) Rubtsov, I. V.; Wang, J.; Hochstrasser, R. M. *J. Chem. Phys.* **2003**, *118*, 7733.
(10) Rubtsov, I. V.; Wang, J. P.; Hochstrasser, R. M. *Proc. Natl. Acad. Sci. U.S.A.* **2003**, *100*, 5601.
(11) Meyer, K. A.; Wright, J. C. *Chem. Phys. Lett.* **2003**, *381*, 642.
(12) Besemann, D.; Meyer, K. A.; Wright, J. C. *J. Phys. Chem. B* **2004**, *108*, 10493.
(13) Meyer, K. A.; Wright, J. C. *J. Phys. Chem. A* **2003**, *107*, 8388.
(14) Hamm, P.; Lim, M.; Hochstrasser, R. M. *J. Phys. Chem. B* **1998**, *102*, 6123.
(15) Hamm, P.; Lim, M.; DeGrado, W. F.; Hochstrasser, R. M. *J. Chem. Phys.* **2000**, *112*, 1907.
(16) Meyer, K. A.; Wright, J. C. *J. Phys. Chem. A* (to be published).
(17) Besemann, D. M.; Condon, N. J.; Murdoch, K. M.; Meyer, K. A.; Zhao, W.; Wright, J. C. *Chem. Phys.* **2001**, *266*, 177.
(18) Mukamel, S. *Principles of Nonlinear Optical Spectrscopy*, 1st ed.; Oxford University Press: New York, 1995.
(19) Zeidler, D.; Frey, S.; Wohlleben, W.; Motzkus, M.; Busch, F.; Chen, T.; Kiefer, W.; Materny, A. *J. Chem. Phys.* **2002**, *116*, 5231.
(20) Zadoyan, R.; Kohen, D.; Lidar, D. A.; Apkarian, V. A. *Chem. Phys.* **2001**, *266*, 323.
(21) Pinkas, I.; Knopp, G.; Prior, Y. *J. Chem. Phys.* **2001**, *115*, 236.
(22) Thompson, D. E.; Merchant, K. A.; Fayer, M. D. *J. Chem. Phys.* **2001**, *115*, 317.
(23) Merchant, K. A.; Thompson, D. E.; Fayer, M. D. *Phys. Rev. A* **2002**, *65*, 023817.
(24) Zhao, W.; Wright, J. C. *Phys. Rev. Lett.* **2000**, *84*, 1411.
(25) Zhao, W.; Wright, J. C. *J. Am. Chem. Soc.* **1999**, *121*, 10994.
(26) Zhao, W.; Wright, J. C. *Phys. Rev. Lett.* **1999**, *83*, 1950.